

SCIENTIFIC REPORTS



OPEN

Damage evaluation in graphene underlying atomic layer deposition dielectrics

Received: 11 February 2015

Accepted: 27 July 2015

Published: 27 August 2015

Xiaohui Tang¹, Nicolas Reckinger^{2,3}, Olivier Poncelet¹, Pierre Louette³, Ferran Ureña¹, Hosni Idrissi^{5,6}, Stuart Turner⁵, Damien Cabosart⁴, Jean-François Colomer^{2,3}, Jean-Pierre Raskin¹, Benoit Hackens⁴ & Laurent A. Francis¹

Based on micro-Raman spectroscopy (μ RS) and X-ray photoelectron spectroscopy (XPS), we study the structural damage incurred in monolayer (1L) and few-layer (FL) graphene subjected to atomic-layer deposition of HfO_2 and Al_2O_3 upon different oxygen plasma power levels. We evaluate the damage level and the influence of the HfO_2 thickness on graphene. The results indicate that in the case of Al_2O_3 /graphene, whether 1L or FL graphene is strongly damaged under our process conditions. For the case of HfO_2 /graphene, μ RS analysis clearly shows that FL graphene is less disordered than 1L graphene. In addition, the damage levels in FL graphene decrease with the number of layers. Moreover, the FL graphene damage is inversely proportional to the thickness of HfO_2 film. Particularly, the bottom layer of twisted bilayer (t-2L) has the salient features of 1L graphene. Therefore, FL graphene allows for controlling/limiting the degree of defect during the PE-ALD HfO_2 of dielectrics and could be a good starting material for building field effect transistors, sensors, touch screens and solar cells. Besides, the formation of Hf-C bonds may favor growing high-quality and uniform-coverage dielectric. HfO_2 could be a suitable high-K gate dielectric with a scaling capability down to sub-5-nm for graphene-based transistors.

One of the most explored application domains for graphene is nanoelectronics because of its high carrier mobility and atomic thickness^{1,2}. However, gate dielectric deposition is an important challenge for transferring graphene transistors from laboratory level to industrial production. Dielectric or metal deposition induces defects in monolayer (1L) graphene and at the interface between dielectric and few-layer (FL) graphene³. The carrier mobility is very sensitive to the graphene lattice defects and interface quality. It has indeed been reported that the carrier mobility of suspended graphene is significantly higher than that of graphene lying over a silicon dioxide (SiO_2) substrate⁴ due to corrugation, traps at the interface and fixed charges in the dielectric layer. Therefore, it is a crucial task to grow metal-oxide dielectric films on graphene with minimum damage/degradation into the graphene lattice.

Although physical vapor deposition (such as magnetron sputtering), widely used in the semiconductor industry, can provide high deposition rates and preserve film stoichiometry, it generates extensive damage in graphene from high energy sputtered atoms⁵. Researchers mostly choose atomic layer deposition

¹ICTEAM Institute, Université catholique de Louvain, Place du Levant 3, 1348 Louvain-la-Neuve, Belgium.

²Research Group on Carbon Nanostructures (CARBONNAGE), University of Namur, Rue de Bruxelles 61, 5000 Namur, Belgium. ³Department of Physics, Research Center in Physics of Matter and Radiation (PMR), University of Namur, Rue de Bruxelles 61, 5000 Namur, Belgium.

⁴NAPS/IMCN, Université catholique de Louvain, 2 Chemin du Cyclotron, 1348 Louvain-la-Neuve, Belgium. ⁵Electron Microscopy for Materials Science (EMAT), Department of Physics, University of Antwerp, Groenenborgerlaan 171, B-2020 Antwerp, Belgium. ⁶Institute of Mechanics, Materials and Civil Engineering, Université catholique de Louvain, Place Sainte Barbe 2, B-1348 Louvain-la-Neuve, Belgium.

Correspondence and requests for materials should be addressed to X.T. (email: xiaohui.tang@uclouvain.be)

(ALD)^{6,7} for dielectric growth on graphene⁸. ALD allows for controlling the thickness and uniformity of the deposited films with atomic-level precision while avoiding physical damage of energized atoms to the surface. ALD techniques are classified into plasma (oxygen-based) and thermal (water-based) depositions. Very few examples dealing with the former technique were reported. Only Nayfeh *et al.*⁹ demonstrated a graphene transistor for which aluminum oxide (Al₂O₃) gate dielectric was directly deposited on graphene by using a remote plasma-enhanced ALD (PE-ALD) process. Most of the reports are related to the latter method, because plasma is rather aggressive (especially using a direct plasma) and generally etches graphene¹⁰. It is well known that graphene is hydrophobic and inert. More specifically, graphene does not provide reactive nucleation sites for the precursors in thermal ALD^{11,12} since it does not display covalent bonds out of the plane. Therefore, growing high-quality and uniform-coverage dielectrics by thermal ALD requires a graphene pretreatment. Various approaches have been proposed: (i) graphene is chemically modified by fluorine¹³, ozone¹⁴, nitride plasma^{15,16}, organic molecules¹⁷ or perylene tetracarboxylic acid^{18,19}; (ii) metal particles are deposited on graphene as appropriate nucleation layers²⁰; (iii) self-assembled monolayers are used to template the direct growth of dielectrics²¹; (iv) graphene islands, serving as a seed layer, are generated by low-power plasma²². Some of these approaches are complicated and incompatible with the existing mainstream integrated circuit technology. More particularly, these approaches might cause undesirable side effects, such as: inducing defects, doping graphene, leaving seed layers, increasing the dielectric thickness, and degrading the dielectric properties. Two previous articles pointed out that graphene is possibly degraded by the pretreatment^{23,24}. Alternatively, the ozone pretreatment has proved to be responsible for significant damage to graphene in high-temperature thermal ALD²⁵.

In this work, we use mild plasma conditions to directly grow hafnium oxide (HfO₂) and Al₂O₃ dielectrics on graphene by PE-ALD. In our process, the graphene samples are placed away from the plasma source for outside of the glow discharge. The remote oxygen plasma with low ion bombardment avoids fast etching of graphene. Simultaneously, the reaction between graphene and the precursor still guarantees physical/chemical modification of graphene. Based on micro-Raman spectroscopy (μ RS) and X-ray photoelectron spectroscopy (XPS), we study the structural damage induced in 1L graphene underlying HfO₂ and Al₂O₃ upon different oxygen plasma power levels. We evaluate the damage levels in AB-stacked bilayer (AB-2L), twisted bilayer (t-BL) and trilayer (3L) graphene (hereafter they are collectively referred to as FL) underlying HfO₂ and Al₂O₃ for a fixed oxygen plasma power. We also investigate the influence of the HfO₂ thickness on graphene with various layer numbers. The results indicate that in the case of Al₂O₃/graphene, both 1L and FL graphene are strongly damaged under the present process conditions. In the case of HfO₂/graphene, μ RS analysis clearly shows that FL graphene presents much less disorder than 1L graphene. Moreover, the FL graphene damage decreases with the number of layers. Our results also reveal that an inverse dependence of FL graphene damage with increasing the thickness of HfO₂ film. FL graphene allows for controlling/limiting the defect formation during the PE-ALD HfO₂ process. Therefore, it could be a good starting material for applications such as graphene-based transistors and sensing devices^{26,27}, since, presently, wafer-scale homogeneous FL graphene can be synthesized by chemical vapor deposition (CVD)²⁸.

Results

Graphene morphology observations by SEM, AFM, optical microscopy and TEM. Figure 1a–c show scanning electron microscopy images of atmospheric pressure chemical vapor deposition (APCVD) graphene on copper foils (see methods and the reference²⁹ for more information about the graphene growth and transfer conditions). The different contrasts in the images correspond to the different graphene layer numbers. It can be seen that the 1L, 2L, and 3L graphene domains are hexagonal. A hexagon is the typical shape of graphene domains grown by APCVD³⁰. In another article, the same group explored the shape variations *versus* the APCVD growth conditions. They explained the shape modulation by the competition between atom diffusion along graphene domain edges or corners and surface diffusion processes³¹. In addition, Fig. 1d presents an atomic force microscopy image of graphene transferred onto SiO₂, in which 1L, 2L and 3L can be clearly seen. Figure 1e plots the profile of stacked graphene flakes along the A–B line, confirming that each graphene layer has a thickness of about 0.3 nm.

Figure 2a illustrates an optical microscopy image of as-transferred graphene on the SiO₂/Si substrate, revealing that the graphene film is composed of isolated and contiguous hexagonal flakes of various layer numbers. Most of the hexagons are 1L. High-angle t-2L, AB-2L and 3L graphene hexagons are found in certain regions. As shown in Fig. 2b, graphene underlying the HfO₂ dielectric film is still clearly visible. Figure 2c shows a cross-sectional high angle annular dark field scanning transmission electron microscopy (HAADF-STEM/Z-contrast) image of the HfO₂/graphene/SiO₂/Si stack, indicating the uniform covering of graphene with the HfO₂ film. No clustering or pinholes in the HfO₂ film is observed.

Graphene structural damage evaluation by μ RS. μ RS is a nondestructive method and is employed here to assess the structural damage in graphene underlying dielectric films. It is worth noting that a laser wave length of 514 nm was used in all the measurements except for the case by special description. Figure 3 shows the Raman spectra of 1L graphene after PE-ALD Al₂O₃ and HfO₂, at an oxygen plasma power of 300 W. The spectra are offset for clarity. For the sake of comparison, the Raman spectrum of as-transferred 1L graphene is also shown at the bottom of the figure. According to the statistical data

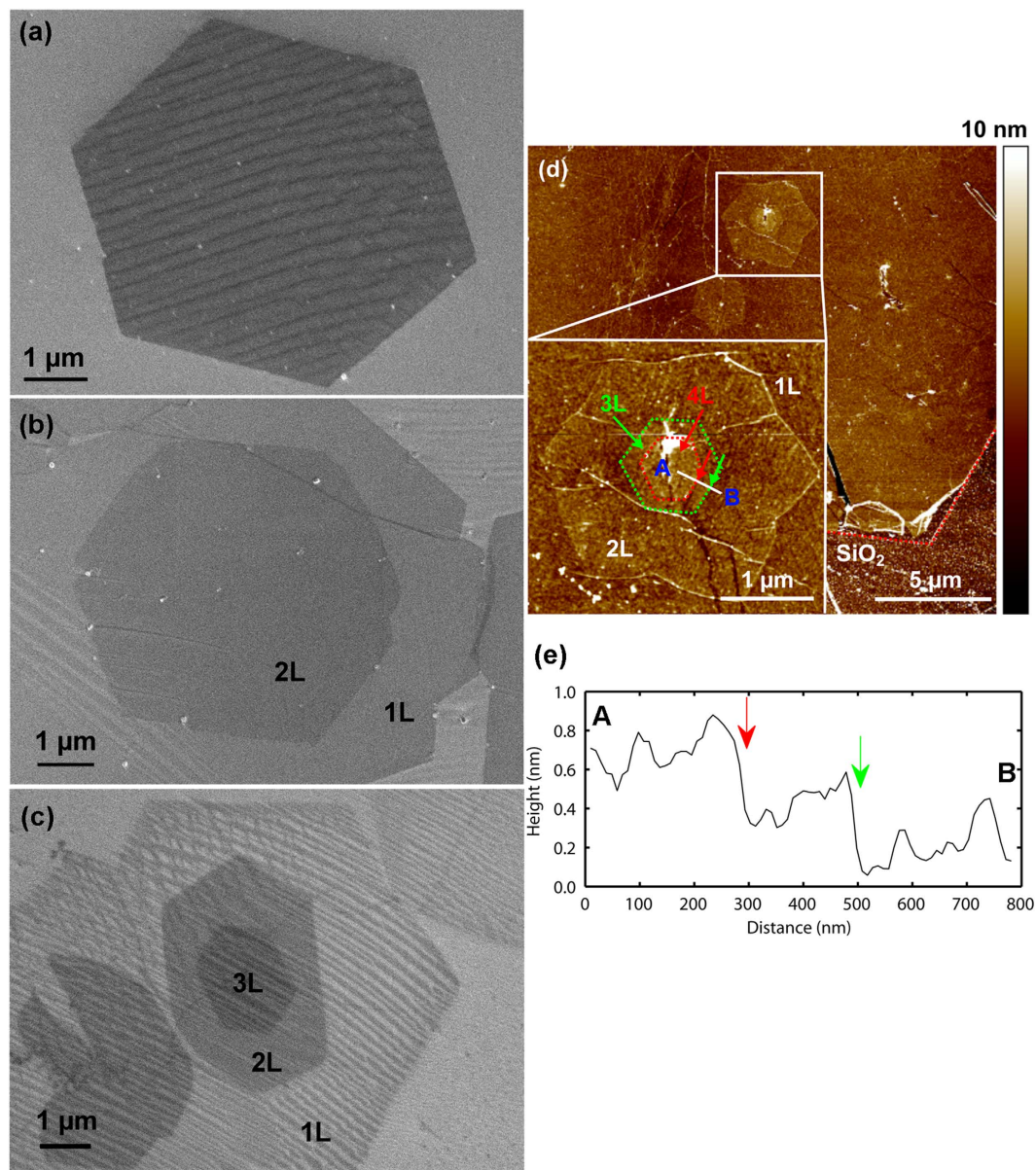


Figure 1. Scanning electron microscopy images for (a) monolayer layer (1L), (b) bilayer (2L), and (c) trilayer (3L) graphene on copper foils. (d) Atomic force microscopy image of as-transferred graphene on SiO₂/Si substrate. (e) Profile of stacked graphene flakes along the A–B line.

from many measured points, the peak at $\sim 1588\text{ cm}^{-1}$ originates from the G mode of graphene. The non-perturbed G mode is usually around 1580 cm^{-1} (see the work of Ferrari *et al.*³²), which is a first order Raman peak related to the E_{2g} optical phonons at the Brillouin zone center. The slight upshift is most probably due to residual strain originating from the copper substrate or/and unintentional doping. The doping possibly comes from traps in the SiO₂ substrate, from insufficient rinsing after copper etching, from PMMA residues in transfer step, from moisture in air, and other similar contamination sources^{33,34,35}. The other peak is the 2D mode at $\sim 2687\text{ cm}^{-1}$, which is a two-phonon second-order Raman process. The integrated intensity ratio (I_{2D}/I_G) is 1.9, and the full width at half maximum (FWHM) of the 2D peak is 31 cm^{-1} . These figures of merit first confirm the presence of as-transferred 1L graphene at the probed locations. At the exact same positions, two new peaks (defect-activated peaks) appear after PE-ALD HfO₂ and PE-ALD Al₂O₃. Namely the D peak located at $\sim 1356\text{ cm}^{-1}$ and the D' peak ($\sim 1620\text{ cm}^{-1}$) at the right shoulder of the G mode. The D peak in sp² graphene is activated by a double resonance Raman process in the presence of disorder and defects and is related to the breathing modes of carbon atoms in the vicinity of the K point in the Brillouin zone (see the work of Ferrari *et al.*³²). The D peak can only be observed when the crystal symmetry is broken by point defects or at the edges of graphene³⁶. The D' mode corresponds to an independent defect-assisted intervalley process in graphene.

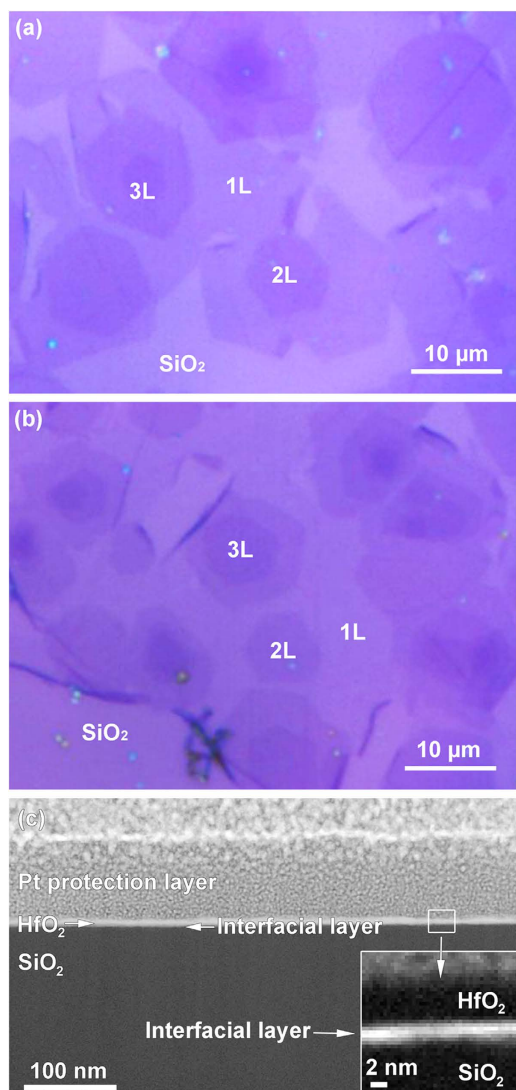


Figure 2. Optical and transmission HAADF-STEM images: (a) as-transferred graphene on SiO₂/Si substrate, (b) HfO₂/graphene/SiO₂/Si stack and (c) cross-section of HfO₂/graphene/SiO₂/Si stack.

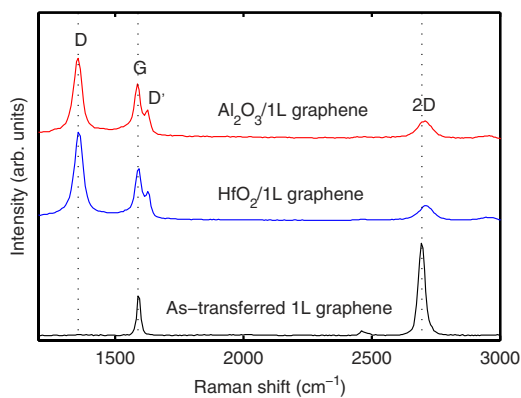


Figure 3. Raman spectra of monolayer graphene without/with PE-ALD HfO₂ and PE-ALD Al₂O₃ films for an oxygen plasma power of 300 W.

It could be due to the presence of sp³ bonding. For as-transferred 1L graphene, the intensity of D peak is weak and ignored, as shown in the bottom spectrum. Since the size of the examined hexagon flake is large enough (larger than 15 μm from vertex to vertex) to make the measurement inside the crystalline

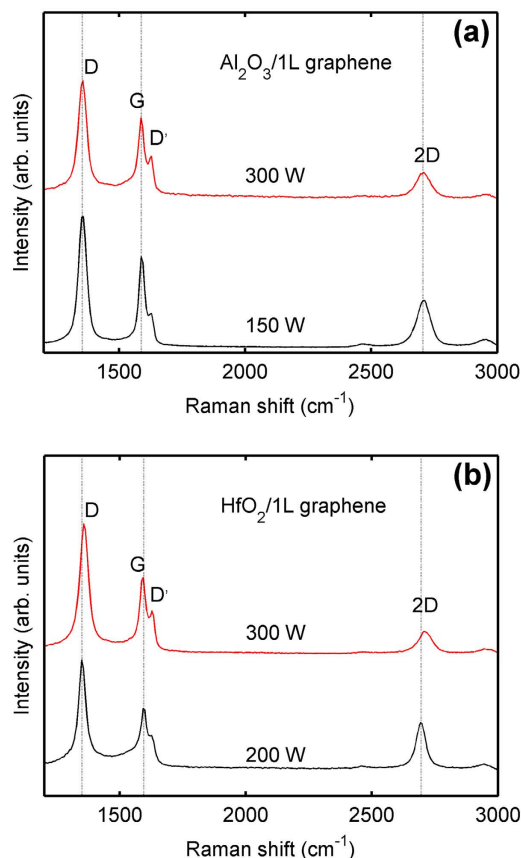


Figure 4. Raman spectra of monolayer graphene covered with (a) PE-ALD Al_2O_3 and (b) PE-ALD HfO_2 for two different oxygen plasma power levels, respectively, (300 or 150 W) and (300 or 200 W).

region (in the center of hexagon) with a Raman laser spot diameter of about $1\ \mu\text{m}$, the boundary of the hexagons does not contribute to the spectrum here. After the dielectric depositions, the intensity of D peaks becomes very strong. This indicates that the dielectric depositions break the symmetry of the graphene lattice and induce structural defects in graphene. Moreover, the positions of the G peaks are slightly shifted, the FWHM of 2D peaks are broadened and the D' peaks are separated from the G peaks. These characteristics indicate that graphene is disordered, but it is not completely etched and then still optically visible. We therefore use the area ratio $A_{D'}/A_G$ between the integrated intensities of the D and G peaks to quantify the amount of disorder (*i.e.* the $A_{D'}/A_G$ increases with increasing amount of disorder at low defect concentration range). The area ratio is preferred over the individual intensities since it accounts for variations in peak position, intensity and linewidth³⁷.

To investigate the damage in graphene subjected to different oxygen plasma power levels, we reduce the oxygen plasma power from 300 to 200 W and 150 W for PE-ALD HfO_2 and PE-ALD Al_2O_3 , respectively. The corresponding Raman spectra of 1L graphene underlying the two dielectrics are shown in Fig. 4a,b, respectively. The D and D' peaks exist even if the oxygen plasma power is reduced to 150 W. The $A_{D'}/A_G$ ratios are very similar for the different power levels (300 and 200 W for HfO_2 , 300 and 150 W for Al_2O_3), implying that the amount of generated disorders in graphene is not correlated to the plasma power levels in this range of powers. For ALD Al_2O_3 on graphene, Lim *et al.* used nitrogen plasma to pretreat graphene³⁸. They investigated the dependence of the number of defects on the nitrogen plasma power levels (30, 60, and 100 W). Their results show that the number of defects is increased with the nitrogen plasma power level. Our results suggest that for oxygen plasma powers above 150 W, the number of defects in 1L graphene has reached saturation.

The layer number is first identified by the color contrast of graphene under optical microscopy, followed by μRS measurements. Figure 5a–d shows the Raman spectra of 3L, AB-2L, t-2L and 1L graphene under HfO_2 and Al_2O_3 with a thickness of about 5 nm, respectively. The Raman spectra of as-transferred graphene with various layer thicknesses (black curves) are also shown at the bottom of the figure as references. In the case of Al_2O_3 /graphene (red curves), all the $A_{D'}/A_G$ ratios are large and all the D' peaks clearly separate from G peaks. These features indicate that all kinds of graphene are damaged during PE-ALD Al_2O_3 . In the case of HfO_2 /3L graphene, the intensity of the D peak becomes very weak and the D' peak even almost disappears (blue curve in Fig. 5a). The $A_{D'}/A_G$ ratios of AB-2L and t-2L graphene are much smaller (blue curves in Fig. 5b,c). However, the spectrum of HfO_2 /1L graphene (blue curve in 5d)

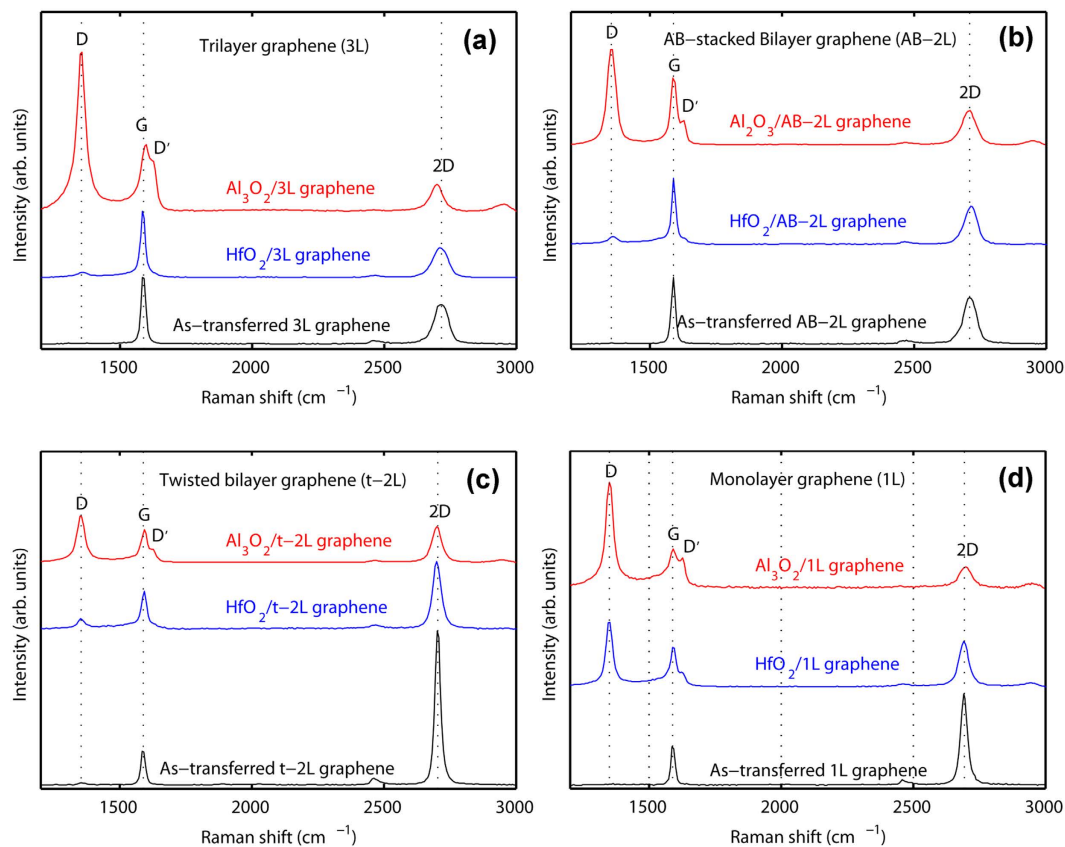


Figure 5. Raman spectra: (a) 3L graphene underlying HfO₂ and Al₂O₃. (b) AB-2L graphene underlying HfO₂ and Al₂O₃. (c) t-2L graphene underlying HfO₂ and Al₂O₃. (d) 1L graphene underlying HfO₂ and Al₂O₃.

is similar to that of the Al₂O₃/graphene case. These results point out that in PE-ALD HfO₂, FL graphene is less damaged than 1L graphene and the damage level of graphene decreases with the number of layers.

We also investigate the influence of the HfO₂ thickness on graphene. Figure 6a–d shows the Raman spectra for 1L, AB-2L, t-2L and 3L graphene under HfO₂ with different thicknesses (0, 0.5, 1 and 5 nm), respectively. It can be seen from Fig. 6a that for different HfO₂ thicknesses, the $A_{D'}/A_G$ ratio of 1L graphene dramatically increases compared with that of as-transferred graphene. However, the changes in the Raman spectra of FL graphene are less drastic. Surprisingly, all the $A_{D'}/A_G$ ratios decrease with increasing the thickness of HfO₂ film (see Fig. 6e). The reason will be discussed later.

Finally, to identify if the HfO₂ film or the hypothesized Hf-C exhibit some peaks in Raman spectra, μ RS analysis is performed using high resolution (1800 gr/mm) gratings and three excitation laser energies in the visible range, namely 514.5 nm (2.41 eV), 488 nm (2.54 eV) and 633 nm (1.92 eV). We do not find any peak related to HfO₂ or Hf-C in the measurement range from 0 to 4000 cm⁻¹. This implies that the HfO₂ film is amorphous due to the low growth temperature.

X-ray photoelectron spectroscopy measurements. We carry out *ex situ* XPS measurements to evaluate the impact of PE-ALD dielectrics on graphene. Four samples are sputtered with an Ar⁺ gun to perform a depth profile: 5.5-nm-thick Al₂O₃ and 5.9-nm-thick HfO₂ are deposited either on silicon (as references) or on graphene/SiO₂/silicon stacks (hereafter referred to as Al₂O₃/silicon, HfO₂/silicon, Al₂O₃/graphene, and HfO₂/graphene, respectively). Core level spectra are recorded from carbon (C 1s), oxygen (O 1s), hafnium (Hf 4f), aluminum (Al 2p), and silicon (Si 2p). The elemental composition of the dielectrics obtained from 20-nm-thick reference layers can be estimated from the ratios of the integrated intensities of the XPS spectra: $[O/Hf] = 2.15 \pm 0.1$ and $[O/Al] = 1.47 \pm 0.05$. These results testify to the good quality of the dielectrics. We now focus on the C 1s atomic concentration profile and spectra of each sample. Figure 7a,b illustrate the depth profiles of the Al₂O₃/silicon and HfO₂/silicon samples, respectively. In both cases, a small amount of carbon (2% on average) is found in the profiles (except for a ~15% concentration corresponding to adventitious carbon on top of the dielectric layers). Moreover, a slight increase of the carbon concentration is observed when approaching the interface between the dielectric and silicon, most likely originating from residual contamination on silicon before PE-ALD. Figure 7c,d display the depth profiles of the Al₂O₃/graphene and HfO₂/graphene samples, respectively.

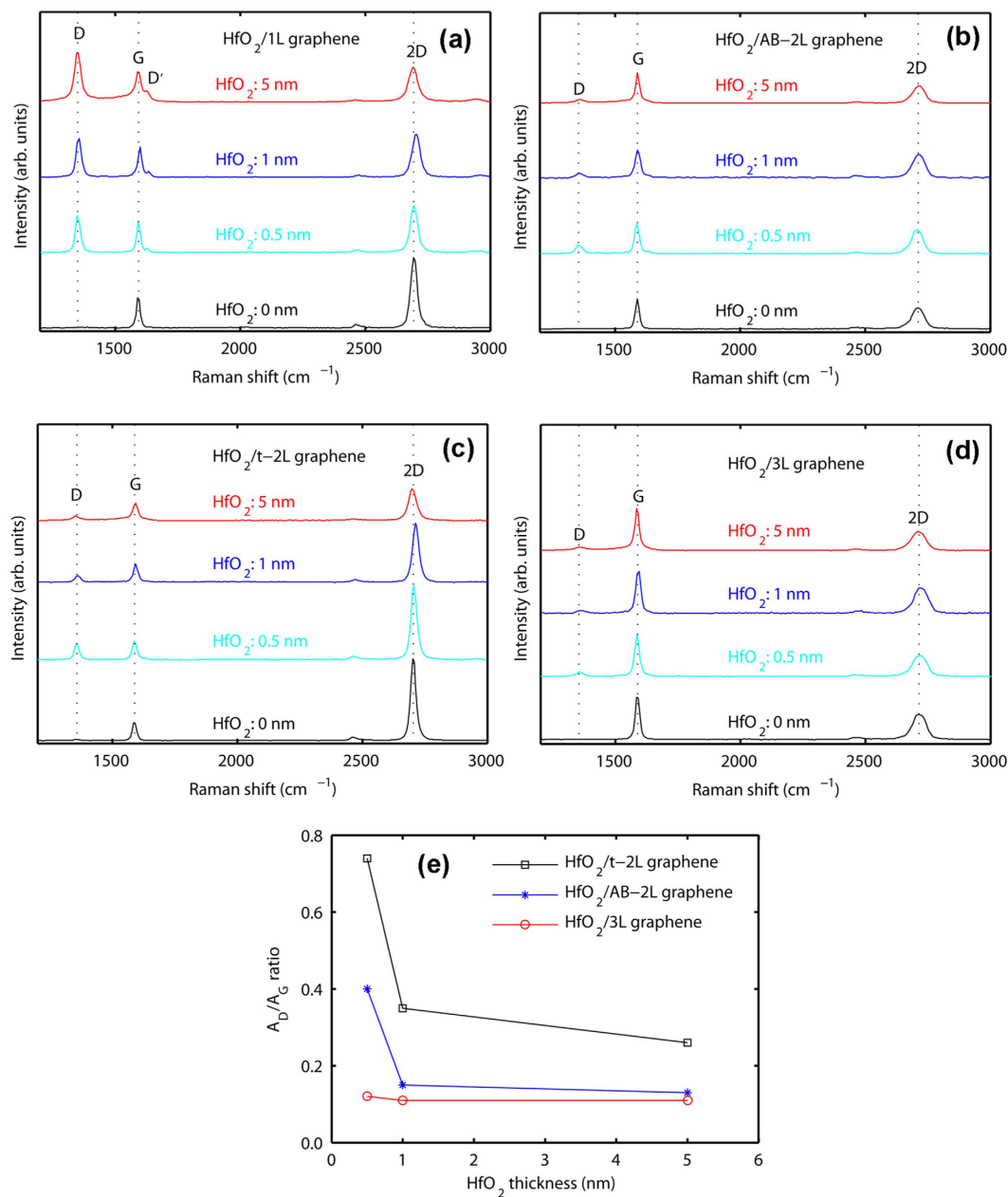


Figure 6. Raman spectra of HfO₂/graphene for graphene layers with thicknesses of HfO₂ (0, 0.5, 1 and 5 nm), (a) 1L, (b) AB-2L, (c) t-2L (t-2L), (d) 3L graphene and (e) all the A_D/A_G ratios as a function of the HfO₂ thickness.

We can clearly identify the presence of graphene between the dielectric and the SiO₂/silicon substrate. Figure 7e,f exhibit the C 1s spectra of the Al₂O₃/graphene and HfO₂/graphene samples at the maximum of the carbon profiles, respectively. The main peak at 284.5 eV in both spectra corresponds to graphene. Strikingly, in contrast to the Al₂O₃/graphene sample, the HfO₂/graphene sample displays an additional peak at 281.5 eV. This peak can be attributed to the formation of the metallic carbide Hf-C. Consequently, the HfO₂/graphene profile in Fig. 7d can be fitted by its two components: C in graphene and C in Hf-C. At the interface, the Hf-C concentration reaches 2% of the total composition (see the cyan and magenta profiles in Fig. 7d, corresponding to C in graphene and C in Hf-C, respectively). However, it was reported by Engelhard *et al.*³⁹ that Ar⁺ sputtering of ALD HfO₂ induces the formation of Hf-C (at an ion-gun energy of 2000 eV), amounting to 1% of the total composition. To ascertain that the observed Hf-C peak is not related to sputtering (the Ar⁺ gun is operated on purpose at the very low energy of 200 eV in the hope of preventing Hf-C formation), we have performed an additional experiment. A 1L graphene is transferred onto an HfO₂/SiO₂/Si substrate and next subjected to sputtering in the same conditions as before. In the corresponding C 1s spectrum, the carbide-related peak occurs as well, most likely due to

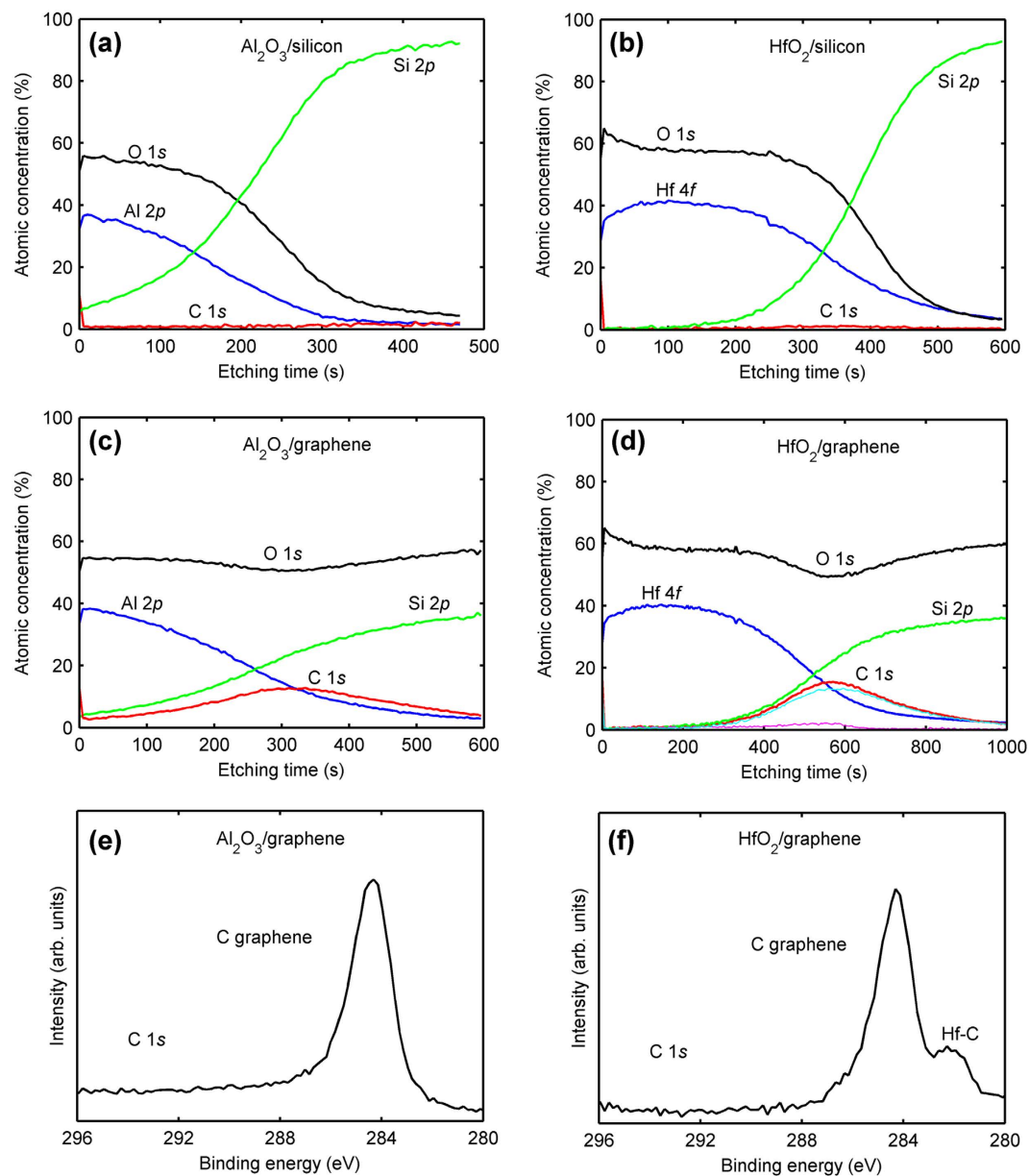


Figure 7. XPS depth profiles of (a) Al₂O₃/silicon, (b) HfO₂/silicon, (c) Al₂O₃/graphene, and (d) HfO₂/graphene samples. C 1s spectra of (e) Al₂O₃/graphene and (f) HfO₂/graphene samples, corresponding to the maximum of the carbon profiles in (c) and (d), respectively.

intermixing between Hf and C during the erosion, resulting in Hf-C bonding. This means that, from the *ex situ* XPS analysis only, we cannot conclude if Hf-C forms during the PE-ALD process or during the erosion process or both. Nonetheless, as opposed to Al-C, this illustrates how easy it is to form Hf-C, since the Ar⁺ sputtering is operated at a very low energy of 200 eV. To further elucidate where Hf-C originates from requires an ALD apparatus fitted with an *in situ* XPS analyzer.

Discussion

Although the optical image of the Al₂O₃/graphene/SiO₂/Si (see Fig. 1 in the Supplementary Information) looks similar to that of the HfO₂/graphene/SiO₂/Si (see Fig. 2), all the graphene samples, regardless of their thickness, are significantly damaged in the PE-ALD Al₂O₃ process (see the Raman spectra of Fig. 5). This may be linked to the fact that the TMA-Al precursor itself does not react with graphene at temperatures lower than 400 °C⁴⁰. Al carbide is not formed during the initial TMA-Al precursor pulse, which is confirmed by the XPS data in Fig. 7e within the detection limits of the technique. This results in a delayed Al₂O₃ nucleation onto graphene. Only when graphene is subjected to the first or few oxidant precursor pulses (which is analogous to a pretreatment by oxygen plasma), the Al₂O₃ film starts to nucleate and then grow. Unfortunately, 1L graphene, and even FL graphene, have been degraded during

the pretreatment. On the contrary, the XPS results have demonstrated that the Hf-C bonds are quite easily formed, whatever the origin of the bonding. We hypothesize that, during the initial TDMA-Hf precursor pulse, a chemical reaction occurs between the Hf atoms and the C atoms constituting graphene to form Hf-C (its formation temperature is 25 °C)³⁹. Hf in Hf-C bonds may act as a uniform and active template for the subsequent HfO₂ growth. Subsequently, the coverage of the first HfO₂ layer protects the underlying graphene layer from damage during the following deposition cycles. This may also explain why HfO₂ rather than Al₂O₃ can be directly grown on graphene without out-of-plane covalent functional groups, in low-temperature thermal ALD process^{41,42}.

On the other hand, the origin of the inverse dependence of the A_D/A_G ratio on the number of graphene layers is not clear. It may be due to the interlayer interactions between the HfO₂ layer and graphene or a direct consequence of the HfO₂ deposition process or both. Previous works about the impact of the graphene thickness on its physical properties suggest that graphene's rigidity may increase with increasing number of layers⁴³. More precisely, when 1L graphene is deposited on top of the SiO₂ substrate, it conforms more easily to the surface morphology of the underlying substrate, thereby more prone to deform compared with FL graphene. Oxygen plasma modification of 2L and FL graphene has been studied in the literature. Calculation results⁴⁴ predict that oxidized 2L graphene, unlike 1L, still retains its intrinsic properties even if the oxygen density is as high as 50%. Electrical experimental results in the work of Felten *et al.*⁴⁵ show that only the top layer of 2L graphene is chemically modified, while the bottom layer maintains its structural integrity. Moreover, it was reported that the chemical modification of FL graphene occurs layer by layer^{46,47}. The Raman spectra of HfO₂/graphene (blue curves in Fig. 5) show that the A_D/A_G ratio of 1L graphene is much larger than that of FL graphene and the D' peak is separated from the G peak in the Raman spectrum of 1L graphene. The formation of Hf-C bonds means a chemical adsorption of Hf atoms on graphene and the conversion of the bond from sp² to sp³, with a resulting increase of the D peak and separation of the D' peak. In addition, the oxygen plasma pulse is very aggressive toward 1L graphene⁴⁸. Besides, the poor rigidity of 1L graphene results in its fracture and wrinkling⁴⁹. All these effects would induce damages in the graphene lattice *e.g.* vacancies, dislocations and dangling bonds. In sharp contrast to 1L, the A_D/A_G ratios of FL graphene significantly decrease. Hf-C bonds are only present on the top layer due to preferential chemisorption of Hf atoms. Since the plasma pulse is less reactive to FL graphene than 1L⁵⁰ and graphene becomes more rigid with the number of layers, this may lead to less damage in FL graphene.

The I_{2D}/I_G ratio and the FWHM of the 2D peak can be used to easily distinguish 1L and t-2L graphene. More specifically, pristine 1L graphene has a I_{2D}/I_G ratio of about 2 and a FWHM of 35 cm⁻¹, while the I_{2D}/I_G ratio and the FWHM of t-2L graphene are about 6 and 28 cm⁻¹, respectively⁵¹. Our results reveal another interesting behavior: after depositing a 5-nm-thick HfO₂ film, t-2L graphene presents "1L-like" features. In other words, when the thickness of the HfO₂ film increases from 0 to 5 nm, the I_{2D}/I_G ratio reduces from 5.83 to 1.97 and the 2D peak FWHM increases from 26 to 38 cm⁻¹ (see Fig. 6c). It is emphasized here that the I_{2D}/I_G ratio of about 2 and the 2D peak FWHM of about 35 cm⁻¹ are the features of 1L graphene³², while t-2L graphene has a I_{2D}/I_G ratio of about 6 and a 2D peak FWHM of about 28 cm⁻¹ (see ref. 51). We suggest that the C atoms in the top layer of t-2L intermixing with Hf atoms and O atoms form an interfacial layer, which is a complex amorphous layer. It is supported by the of the cross-sectional HAADF-STEM image as shown in the insert of Fig. 2c. This is consistent with a previous work⁵². In Fig. 6c, we can see that the spectrum of t-2L gradually becomes 1L-like upon augmenting the HfO₂ thickness. We make the assumption that, below 5 nm, the interfacial layer is not completely formed. In contrast, for 5 nm, the top graphene layer is entirely incorporated into the interfacial layer, leaving a stack made up of HfO₂/amorphous interlayer/1L-like graphene. μ RS cannot detect that interfacial layer because it is amorphous. On the other hand, Felten *et al.*⁴⁵ observed a similar behavior with AB-2L under different plasma conditions. Indeed, they show by electrical measurements that after long-time and mild plasma treatment, 1L becomes an insulator, while AB-2L graphene still retains its ambipolar property with a relatively high charge mobility. They attribute these facts to the chemically modified top graphene layer and decoupling between the top and bottom layer. However, we did not observe the same behavior for AB-2L and 3L.

As shown in Fig. 6e, the A_D/A_G ratios of FL graphene decrease with increasing the thickness of HfO₂. This is also consistent with the above discussions. More specifically, the increase of the HfO₂/graphene thickness makes it more difficult to conform to the surface morphology of the underlying substrate, and as a consequence graphene is less prone to deform.

It is worth emphasizing that FL graphene may be a prospective material with regard to applications such as transistors and sensors. For instance, it has been reported that the sheet resistance of 2L graphene is smaller than that of 1L graphene and the low-frequency 1/f noise in the transistor (30-nm gate length) made from 2L graphene is strongly suppressed compared with 1L graphene transistors^{53,54}.

Conclusion

We have investigated the structural damage in graphene underlying dielectrics (HfO₂ and Al₂O₃) deposited by remote PE-ALD. Our results show that FL graphene is less damaged than 1L graphene; the damage level of FL graphene decreases not only with the number of graphene layers but also with the thickness of HfO₂. Interestingly, the Raman spectrum of t-2L graphene underlying HfO₂ presents the features of that of as-transferred 1L graphene. XPS measurements indicate that Hf-C is easily formed. After

Dielectric Name	HfO ₂	Al ₂ O ₃
Precursor acronym	TDMA-Hf	TMA
Precursor chemical formula	[(CH ₃) ₂ N] ₄ Hf	Al ₂ (CH ₃) ₆
Precursor temperature (°C)	75	25
Precursor pulse duration (s)	0.25	0.06
Cycle number (cycle)	55	55
Final thickness (nm)	5.9	5.5

Table 1. Process conditions in PE-ALD and thicknesses of the two dielectric films.

coverage by the first HfO₂, the bottom graphene layer has an additional protection. The oxygen plasma pulse in PE-ALD is less reactive to FL graphene than 1L. Graphene rigidity increases with the number of graphene layers. Moreover, it also increases with the thickness of HfO₂. These may be the reasons of FL graphene less damaged in PE-ALD HfO₂. Therefore, FL graphene, more particularly, t-2L graphene allows for controlling/limiting the defect formation during the PE-ALD HfO₂ process and might be a prospective material for applications such as graphene-based transistors and sensing devices. It appears that the thickness of PE-ALD HfO₂ can be arbitrarily scaled down to 5 nm. Our results open up direct perspectives for FL graphene and HfO₂ gate dielectric in graphene-based transistor applications.

Methods

APCVD graphene conditions. Graphene is synthesized by APCVD with dilute methane (5% in argon) as hydrocarbon precursor on copper foils (Alfa Aesar #13382). The samples are grown at 1000 °C for 1 h under flows of 500 sccm of argon, 20 sccm of hydrogen, and 0.2 sccm of dilute methane. Graphene is then transferred onto 300-nm-thick SiO₂/Si substrates (to easily observe graphene with a conventional white light microscope) by the usual method based on PMMA, after etching the copper foil in ammonium persulfate.

Process conditions for PE-ALD of dielectrics on graphene. HfO₂ and Al₂O₃ films are deposited on graphene/SiO₂/Si stacks, by PE-ALD (Fiji F200 from Ultratech/Cambridge NanoTech Inc., MA) at 250 °C. The plasma source, inductively coupled at 13.56 MHz, is far away from the samples. It is very important to note that the distance between the plasma source and sample location is larger than 40 cm since the type and concentration of the reactive species (electrons, ions, and radicals) strongly depend on this distance. Outside of the glow discharge, only long lifetime radicals are present while ions and electrons recombine quickly.

In order to remove the native stress and polymethyl methacrylate (PMMA) residues from growth and transfer, the graphene samples on the SiO₂/Si substrate first are annealed at 250 °C for 2 h in the deposition chamber under pressure of 80 mtorr (argon gas). During both dielectric film depositions, the pulse duration of the oxygen plasma (oxidant precursor) is 10 s for each cycle. The flows of the oxygen plasma and the argon carrier gas are 20 and 200 sccm, respectively. The metallic and oxidant precursor pulses are separated by a short argon purge of 5 s. To obtain uniform dielectric films and avoid graphene etching, the metallic precursors are first pulsed on the graphene surface. The metallic precursors can adsorb or react with carbon to form the related metal oxides following the first oxidant precursor pulse. In contrast, if the first pulse is a single cycle of oxygen plasma, the graphene surface is possibly damaged or non-uniform dielectric films are formed. The other parameters related to the metallic precursors and the final thickness of both dielectric films are listed in Table 1. The thickness of the dielectric films is measured by *in situ* ellipsometry from reference films directly deposited on silicon substrates. The composition of the dielectric films is characterized by XPS. In order to investigate the damage level of graphene upon different oxygen plasma power levels, HfO₂ and Al₂O₃ films are deposited on graphene/SiO₂/Si stacks with nominal 300 W and with reduced oxygen plasma power of 200 and 150 W, respectively.

Raman spectroscopy system. A LabRam HR 800 confocal laser system from Horiba Jobin Yvon was used for the acquisition of the Raman spectra. The measurements are performed at room temperature with a laser wavelength $\lambda = 514$ nm in backscattering geometry. The laser beam is focused on the center of hexagons and a 100 × objective (NA = 0.95) is used to collect the signal. The incident power is kept below 1 mW. Low resolution (150 g/mm) and high resolution (1800 g/mm) gratings are used for the measurements.

XPS characterization. A ThermoFisher Scientific K-alpha spectrometer is employed. It is equipped with a monochromatized Al K $\alpha_{1,2}$ x-ray source and a hemispherical deflector analyzer. The spectra are recorded at constant pass energy (150 eV for depth profiling and survey; 30 eV for high resolution spectra). A flood gun (low energy electrons and Ar ions) is used during all the measurements. During the sputtering, the Ar⁺ ion gun is operated at a low energy (200 eV), with an erosion time of 5 s per cycle,

and the analysis is done in snapshot mode. The XPS data are treated with the Avantage software. High resolution spectra are fitted by Gaussian-Lorentzian lineshapes with an Avantage “smart” background (*i.e.* a Shirley background in most cases, or a linear background in case the lineshape decreases with increasing BE).

References

1. Avouris, P. Graphene: electronic and photonic properties and devices. *Nano Lett.* **10**, 4285–4294 (2010).
2. Novoselov, K. S. *et al.* A roadmap for graphene. *Nature* **490**, 192–200 (2012).
3. Jin, Z., Su, Y., Chen, J., Liu, X. & Wu, D. Study of AlN dielectric film on graphene by Raman microscopy. *Appl. Phys. Lett.* **95**, 233110 (2009).
4. Novoselov, K. S. *et al.* Electric field effect in atomically thin carbon films. *Science* **306**, 666–669 (2004).
5. Chen, C.-T., Casu, E. A., Gajek, M. & Raoux, S. Low-damage high-throughput grazing-angle sputter deposition on graphene. *Appl. Phys. Lett.* **103**, 033109 (2013).
6. Ganapathi, K. L., Bhat, N. & Mohan, S. Optimization of HfO₂ films for high transconductance back gated graphene transistors. *Appl. Phys. Lett.* **103**, 073105 (2013).
7. Yu, M., Yuan, W., Li, C., Hong, J.-D. & Shi, G. Performance enhancement of a graphene–sulfur composite as a lithium–sulfur battery electrode by coating with an ultrathin Al₂O₃ film via atomic layer deposition. *J. Mater. Chem. A*, **2**, 7360 (2014).
8. Lee, B. *et al.* Conformal Al₂O₃ dielectric layer deposited by atomic layer deposition for graphene-based nanoelectronics. *Appl. Phys. Lett.* **92**, 203102 (2008).
9. Nayfeh, O. M., Marr, T. & Dubey, M. Impact of plasma-assisted atomic-layer-deposited gate dielectric on graphene transistors. *IEEE Electron Device Lett.* **32**, 473–475 (2011).
10. Wu, Y. Q. *et al.* Top-gated graphene field-effect-transistors formed by decomposition of SiC. *Appl. Phys. Lett.* **92**, 092102 (2008).
11. Addou, R., Dahal, A. & Batzill, M. Growth of a two-dimensional dielectric monolayer on quasi-freestanding graphene. *Nat. Nanotechnol.* **8**, 41–45 (2013).
12. Wang, X., Tabakman, S. M. & Dai, H. Atomic layer deposition of metal oxides on as-transferred and functionalized graphene. *J. Am. Chem. Soc.* **130**, 8152–8153 (2008).
13. Wheeler, V. *et al.* Fluorine functionalization of epitaxial graphene for uniform deposition of thin high- κ dielectrics. *Carbon* **50**, 2307–2314 (2012).
14. Jandhyala, S. *et al.* Atomic layer deposition of dielectrics on graphene using reversibly physisorbed ozone. *ACS Nano* **6**, 2722–2730 (2012).
15. Lin, Y.-M. *et al.* Operation of graphene transistors at gigahertz frequencies. *Nano Lett.* **9**, 422–426 (2009).
16. Wang, L. *et al.* Ultrathin oxide films by atomic layer deposition on graphene. *Nano Lett.* **12**, 3706–3710 (2012).
17. Alaboson, J. M. P. *et al.* Seeding atomic layer deposition of high- k dielectrics on epitaxial graphene with organic self-assembled monolayers. *ACS Nano* **5**, 5223–5232 (2011).
18. Robinson, J. A. *et al.* Epitaxial graphene materials integration: effects of dielectric overlayers on structural and electronic properties. *ACS Nano* **4**, 2667–2672 (2010).
19. Tselev, A. *et al.* Near-field microwave microscopy of high- κ oxides grown on graphene with an organic seeding layer. *Appl. Phys. Lett.* **103**, 243105 (2013).
20. Fallahzad, B. *et al.* Scaling of Al₂O₃ dielectric for graphene field-effect transistors. *Appl. Phys. Lett.* **100**, 093112 (2012).
21. Justice, M. P. A. *et al.* Templating sub-10 nm atomic layer deposited oxide nanostructures on graphene via one-dimensional organic self-assembled monolayers. *Nano Lett.* **13**, 5763–5770 (2013).
22. Shin, W. C., Bong, J. H., Choi, S.-Y. & Cho, B. J. Functionalized graphene as an ultrathin seed layer for the atomic layer deposition of conformal high- k dielectrics on graphene. *ACS Appl. Mater. Interfaces* **5**, 11515–11519 (2013).
23. Dlubak, B. *et al.* Are Al₂O₃ and MgO tunnel barriers suitable for spin injection in graphene? *Appl. Phys. Lett.* **97**, 092502 (2010).
24. Qiu, X. P. *et al.* Disorder-free sputtering method on graphene. *AIP Adv.* **2**, 032121 (2012).
25. Lee, B. *et al.* Characteristics of high- k Al₂O₃ dielectric using ozone-based atomic layer deposition for dual-gated graphene devices. *Appl. Phys. Lett.* **97**, 043107 (2010).
26. Park, S. J. *et al.* Ultrasensitive flexible graphene based field-effect transistor (FET)-type bioelectronic nose. *Nano Lett.* **12**, 5082–5090 (2012).
27. Rao, F. B., Almumen, H., Fan, Z., Li, W. & Dong, L. X. Inter-sheet-effect-inspired graphene sensors: design, fabrication and characterization. *Nanotechnology* **23**, 105501 (2012).
28. Lee, S., Lee, K. & Zhong, Z. Wafer scale homogeneous bilayer graphene films by chemical vapor deposition. *Nano Lett.* **10**, 4702–4707 (2010).
29. Reckinger, N., Felten, A., Santos, C. N., Hackens, B. & Colomer, J.-F. The influence of residual oxidizing impurities on the synthesis of graphene by atmospheric pressure chemical vapor deposition. *Carbon* **63**, 84–91 (2013).
30. Wu, B. *et al.* Equiangular Hexagon-Shape-Controlled Synthesis of Graphene on Copper Surface. *Adv. Mater.* **23**, 3522–3525 (2011).
31. Wu, B. *et al.* Self-organized graphene crystal patterns. *NPG Asia Mater* **5**, e36 (2013).
32. Ferrari, A. C. & Basko, D. M. Raman spectroscopy as a versatile tool for studying the properties of graphene. *Nat. Nanotechnol.* **8**, 235–246 (2013).
33. Huang, M., Yan, H., Heinz, T. F. & Hone, J. Probing strain-induced electronic structure change in graphene by Raman spectroscopy. *Nano Lett.* **10**, 4074–4079 (2010).
34. Casiraghi, C., Pisana, S., Novoselov, K. S., Geim, A. K. & Ferrari, A. C. Raman fingerprint of charged impurities in graphene. *Appl. Phys. Lett.* **91**, 233108 (2007).
35. Kalbac, M. *et al.* The influence of strong electron and hole doping on the Raman intensity of chemical vapor-deposition graphene. *ACS Nano* **4**, 6055–6063 (2010).
36. Ferrari, A. C. Raman spectroscopy of graphene and graphite: disorder, electron–phonon coupling, doping and nonadiabatic effects. *Solid State Commun.* **143**, 47–57 (2007).
37. Basko, D. M., Piscanec, S. & Ferrari, A. C. Electron–electron interactions and doping dependence of the two-phonon Raman intensity in graphene. *Phys. Rev. B*, **80**, 165413 (2009).
38. Lim, T., Kim, D. & Ju, S. Direct deposition of aluminum oxide gate dielectric on graphene channel using nitrogen plasma treatment. *Appl. Phys. Lett.* **103**, 013107 (2013).
39. Engelhard, M., Herman, J., Wallace, R. & Baer, D. As-received, ozone cleaned and Ar⁺ sputtered surfaces of hafnium oxide grown by atomic layer deposition and studied by XPS. *Surf. Sci. Spectra* **18**, 46–57 (2011).
40. Pirkle, A., Wallace, R. B. & Colombo, L. *In situ* studies of Al₂O₃ and HfO₂ dielectrics on graphite. *Appl. Phys. Lett.* **95**, 133106 (2009).

41. Meric, I. *et al.* Current saturation in zero-bandgap, top-gated graphene field-effect transistors. *Nat. Nanotechnol.* **3**, 654–659 (2008).
42. Zou, K., Hong, X., Keefer, D. & Zhu, J. Deposition of high-quality HfO₂ on graphene and the effect of remote oxide phonon scattering. *Phys. Rev. Lett.* **105**, 126601 (2010).
43. Gupta, A., Chen, G., Joshi, P., Tadigadapa, S. & Eklund, P. C. Raman scattering from high-frequency phonons in supported n-graphene layer films. *Nano Lett.* **6**, 2667–2673 (2006).
44. Nourbakhsh, A. *et al.* Single layer vs bilayer graphene: a comparative study of the effects of oxygen plasma treatment on their electronic and optical properties. *J. Phys. Chem. C.* **115**, 16619–16624 (2011).
45. Felten, A. *et al.* Single- and double-sided chemical functionalization of bilayer graphene. *Small* **9**, 631–639 (2013).
46. Luo, Z. *et al.* Thickness-dependent reversible hydrogenation of graphene layers. *ACS Nano* **3**, 1781–1788 (2009).
47. Gokus, T. *et al.* Making graphene luminescent by oxygen plasma treatment. *ACS Nano* **3**, 3963–3968 (2009).
48. Ryu, S., Maultzsch, J., Han, M. Y., Kim, P. & Brus, L. E. Raman spectroscopy of lithographically patterned graphene nanoribbons. *ACS Nano* **5**, 4123–4130 (2011).
49. Ni, Z. H. *et al.* Tunable stress and controlled thickness modification in graphene by annealing. *ACS Nano* **2**, 1033–1039 (2008).
50. Jaiswal, M. *et al.* Controlled hydrogenation of graphene sheets and nanoribbons. *ACS Nano* **5**, 888–896 (2011).
51. Fang, W. *et al.* Rapid identification of stacking orientation in isotopically labeled chemical-vapor grown bilayer graphene by Raman spectroscopy. *Nano Lett.* **13**, 1541–1548 (2013).
52. Zhou, P. *et al.* Direct deposition of uniform high-k dielectrics on graphene. *Sci. Rep.* **4**, 6448 (2014).
53. Lin, Y.-M. & Avouris, P. Strong suppression of electrical noise in bilayer graphene nanodevices. *Nano Lett.* **8**, 2119–2125 (2008).
54. Liu, J., Rumyantsev, S., Shur, M. S. & Balandin, A. A. Origin of 1/f noise in graphene multilayers: surface vs. volume. *Appl. Phys. Lett.* **102**, 093111 (2013).

Acknowledgments

The authors thank the staff of UCL's Winfab and Welcome for technical support. Xiaohui Tang is a senior research of UCL. This work is financially supported by the Multi-Sensor-Platform for Smart Building Management project (No. 611887) and the Action de Recherche Concertée (ARC) “StressTronics”, Communauté française de Belgique. Part of this work is financially supported by the Belgian Fund for Scientific Research (FRS-FNRS) under FRFC contract “Chemographene” (No. 2.4577.11). J.-F. Colomer and B. Hackens are Research Associates of FRS-FNRS. This research used resources of the Electron Microscopy Service located at the University of Namur (“Plateforme Technologique Morphologie – Imagerie”). This research used resources of the ELISE Service of the University of Namur. This Service is member of the “Plateforme Technologique SIAM”. The research leading to this work has received partial funding from the European Union Seventh Framework Program under grant agreement No 604391 Graphene Flagship.

Author Contributions

X.T. designed the experiment and wrote the manuscript. N.R. synthesized graphene, took the SEM pictures, and transferred graphene on SiO₂ substrates. X.T. and O.P. performed the PE-ALD. N.R. and X.T. performed the Raman measurements. X.T. and F.U. analyzed the Raman data. N.R. and P.L. performed the XPS and analyzed the results. H.I. and S.T. took the TEM pictures. D.C. provided the AFM images and analysis. J.-F.C., J.-P.R., B.H. and L.F. discussed the results. All authors reviewed the manuscript.

Additional Information

Supplementary information accompanies this paper at <http://www.nature.com/srep>

Competing financial interests: The authors declare no competing financial interests.

How to cite this article: Tang, X. *et al.* Damage evaluation in graphene underlying atomic layer deposition dielectrics. *Sci. Rep.* **5**, 13523; doi: 10.1038/srep13523 (2015).



This work is licensed under a Creative Commons Attribution 4.0 International License. The images or other third party material in this article are included in the article's Creative Commons license, unless indicated otherwise in the credit line; if the material is not included under the Creative Commons license, users will need to obtain permission from the license holder to reproduce the material. To view a copy of this license, visit <http://creativecommons.org/licenses/by/4.0/>